Dynamic response of Advanced Placed Ply composites

Dynamic response of Advanced Placed Ply composites

Rutger Kok[1], Marco Peroni[2], Francisca Martinez-Hergueta[1]*, Antonio Pellegrino[3]

[1] *School of Engineering, Institute for Infrastructure and Environment, The University of Edinburgh, William Rankine Building, EH9 3FG, Edinburgh, United Kingdom*
[2] *European Commission, Joint Research Center, Ispra, Italy*
[3] *University of Oxford, Department of Engineering Science, Parks Road, OX1 3PJ, Oxford, United Kingdom*

**francisca.mhergueta@ed.ac.uk*

Abstract

This work investigates the high strain rate behavior of AP-PLY composites. The large representative volume elements and brittle nature of this material necessitated the use of a bespoke split-Hopkinson bar apparatus. AP-PLY and baseline laminates were subjected to tensile loading at strain rates of 30 s^{-1}. Results were compared with quasi-static data to evaluate whether the laminate architecture introduced any strain rate dependency. In addition, the dynamic experiments were simulated using a multiscale modeling framework, providing further insights into the micromechanisms governing material behavior. The moduli of the AP-PLY composites were found to be strain rate independent, however, strengths were found to be marginally higher than those of their baseline counterparts. At high strain rates, the strain concentrations induced by the geometry of the individual tapes at through thickness undulations and tow boundaries were less significant due to reduced out-of-plane tow straightening and delamination. As a result, no reduction in AP-PLY strength in comparison to the baseline laminates was obtained. These differences in deformation micromechanisms led to an improvement of the damage tolerance when subjected to dynamic loading.

Keywords: Impact behaviour, Automated fiber placement lay-up, 3-Dimensional reinforcement, computational modelling

1. Introduction

Advanced Placed Ply (AP-PLY) is a novel preforming method for Automated Fiber Placement (AFP) that creates through thickness reinforcements by interlacing fiber tows in a pseudo-woven architecture [1, 2, 3, 4, 5]. The three-dimensional reinforcements improve the impact damage tolerance of AP-PLY composites while allowing them to retain the excellent stiffness and strength of conventional angle ply laminates. Previous studies have reported significant improvements in mode I interlaminar fracture toughness and compression after impact (CAI) strength as a result of this novel preforming method [1]. As such, AP-PLY composites are potentially a suitable material choice for aerospace components susceptible to dynamic loads such as engine blades, brackets, nacelles, propellers/rotors, turbine casings, and wings. Previous studies have investigated the low and high velocity impact performance of AP-PLY composites [1, 6, 7, 8]. However, due to the experimental difficulties associated with large representative volume elements (RVEs), the in-plane dynamic material properties of this new family of composite materials has yet to be investigated.

The strain rate dependency of composites is typically characterized using Split Hopkinson Bar (SHB) experiments, which provide the stress-strain curves of a material at different strain rates [9]. The high strain rate behavior of conventional carbon fiber epoxy composites has been extensively studied. Fiber dominated material properties are generally strain rate independent, while matrix dominated deformation and failure modes are highly sensitive to changes in the strain rate [10, 11, 12, 13]. The strain rate dependency of composites containing 3D reinforcements is, however, less well understood [10, 14, 15, 16, 17].

Reliable data on the dynamic properties of AP-PLY composites are sparse mainly due to experimental difficulties [18]. Conventional SHBs are limited to specimens with relatively small dimensions, however, the large representative volume elements of AP-PLY composites (approximately 40 mm x 40 mm) require the use of more advanced non standard equipment. First, exceptionally large bar diameters and pulse magnitudes are required to generate forces sufficient to break the specimens. Second, a large pulse duration with a progressive rising time is required to avoid the premature failure of the brittle composite [19]. An additional consequence of the brittle nature of carbon fiber composites is that they are more sensitive to mechanical gripping, which may result in measurements of strength that underestimate the actual material strength [20]. Furthermore, since the gauge length and distance between bar ends are much greater in large SHBs, it is more difficult to achieve force equilibrium, requiring more detailed analysis to ascertain the validity of the experimental data [21]. In summary, characterizing the tensile high strain-rate behavior of brittle materials with large RVEs, such as AP-PLY composites, using specimen sizes representative of global material behavior, is highly demanding, both in terms of equipment and data processing expertise.

In this context, numerical simulations can be used in tandem with experiments to characterize the dynamic material properties. This methodology mitigates the uncertainties arising from boundary-conditions [22, 23] and can provide valuable insights into the triggering sequence of failure mechanisms that can not be captured experimentally due to the space and time-resolution limitations of high-speed imaging techniques and post-mortem fractography [12]. In this study, the high strain rate mechanical properties of AP-PLY composites are determined using a hybrid experimental and numerical approach. The response of the AP-PLY laminates is compared with those of conventional angle ply composites to quantify the effect of the through thickness fiber undulations. Section 2 summarizes the manufacturing process for these novel composites, and Section 3 details the experimental setup, including post-processing of the data from the split-Hopkinson bar apparatus. Section 4 provides a brief overview of the previously validated 3D multiscale numerical framework used to model the response of the AP-PLY laminates. Section 5 analyzes the behavior of the AP-PLY laminates at high strain rates, on the basis of the combined numerical and experimental results.

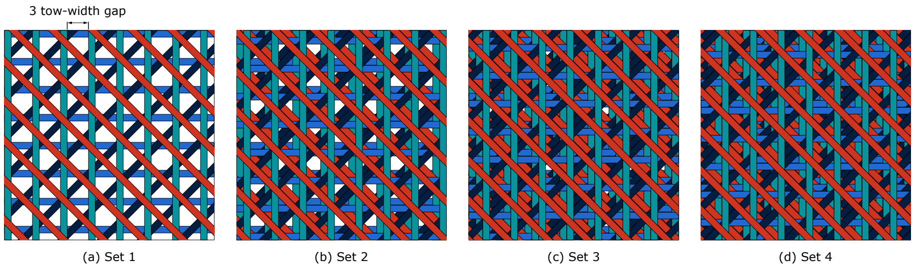

Figure 1: Schematic illustration of the layup process for the quasi-isotropic AP-PLY laminate. Following steps (a) through (d) produces in a 4 ply laminate. To produce the 32-ply thick laminate used in this study, steps (a) through (d) were completed 4 times, and then the process was repeated (4 times) in reverse to produce a symmetric laminate.

2. Materials

Two AP-PLY laminates were manufactured, one cross-ply $[0/90]_{5s}$ ($\mathrm{XP}_{\text{AP-PLY}}$) and one quasi-isotropic $[0/45/90/\text{-}45]_{4s}$ ($\mathrm{QI}_{\text{AP-PLY}}$). The latter represents the state of the art in terms of the geometrical complexity of its internal architecture [2, 24, 25]. Each AP-PLY laminate was laid up by hand. Tows with a width of 10 mm were first slit from a roll of prepreg (SHD Composites VTC401), then placed into a mould according to a predefined layup sequence. To ensure the correct alignment of each tow, guides were printed. Figure 1 illustrates the layup process for the quasi-isotropic AP-PLY laminate. In both laminates a gap of three tow widths was left between tows placed in the same set. The 300 mm x 300 mm panels were cured in a hot press under 4 bars of pressure at 120°C for 120 minutes. In addition, two reference – non AP-PLY – laminates were manufactured for comparison with the AP-PLY panels, (XP_{ref} and QI_{ref}). The AP-PLY preforming process did not alter the thickness of laminates. The average quasi-isotropic specimen thicknesses were 6.95±0.15 mm and 6.88±0.04 mm for the AP-PLY and baseline configurations respectively. For the cross-ply configuration, the average AP-PLY specimen thickness was 4.14±0.05 mm, while the average baseline specimen thickness was 4.20±0.16 mm.

Specimens were extracted from the laminates using computerized numerical control (CNC) machining according to the design reported in Figure 2. The width of the gauge section varied between 30 mm and 40 mm to ensure the response was representative of the mechanical behavior of the parent laminates [5]. Aluminium end tabs were adhered to the specimens to improve stress transfer between the clamps and the specimen. The end tabs were extracted using a water jet and adhered to the specimens using a two part epoxy adhesive (Permabond ET5428). Clamps were used to provide a consolidating pressure while the adhesives cured in an oven according to the manufacturer's recommended cure cycle (60°C for 1 hour). Excess adhesive was removed by machining to achieve the desired dimensional tolerances for testing.

3. Experimental Techniques

The experimental campaign was carried out at the facilities of the European Laboratory for Structural Assessment: Large Hopkinson Bar Facility (ELSA-HopLab) [26]. The Split Hopkinson

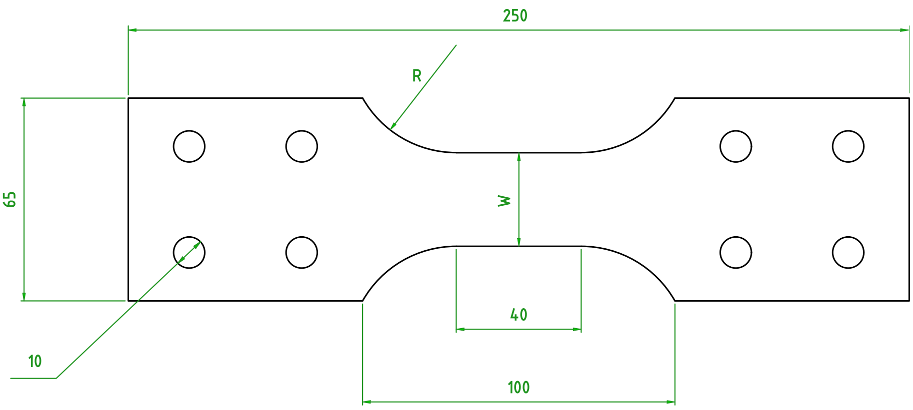

Figure 2: Dynamic tensile testing specimen dimensions (in mm).

Bar (SHB) at the HopLab facility consists of incident and transmitter bars made of steel, 72 mm in diameter and 12 m and 90 m in length respectively, see Fig. 3. It is the world's largest Hopkinson Bar, specifically designed to test components, sub-assemblies and large material samples. Loading pulses were generated by first pretensioning a steel cable, then suddenly releasing it using explosive bolts. This generated a stress pulse with an input velocity of 5 m/s and an approximate effective strain rate of 30 s^{-1}. The specimens had a gauge length of 40 mm and were threaded into the bars with custom clamps, see Fig 4(b). Four M10 bolts provided sufficient clamping force to prevent slippage of the specimens. The friction coefficient between the specimen and the clamps was further increased by knurling the surface of the grips. Four pins were used to prevent any movement between the upper and lower clamp plates. A minimum of six specimens per configuration were tested.

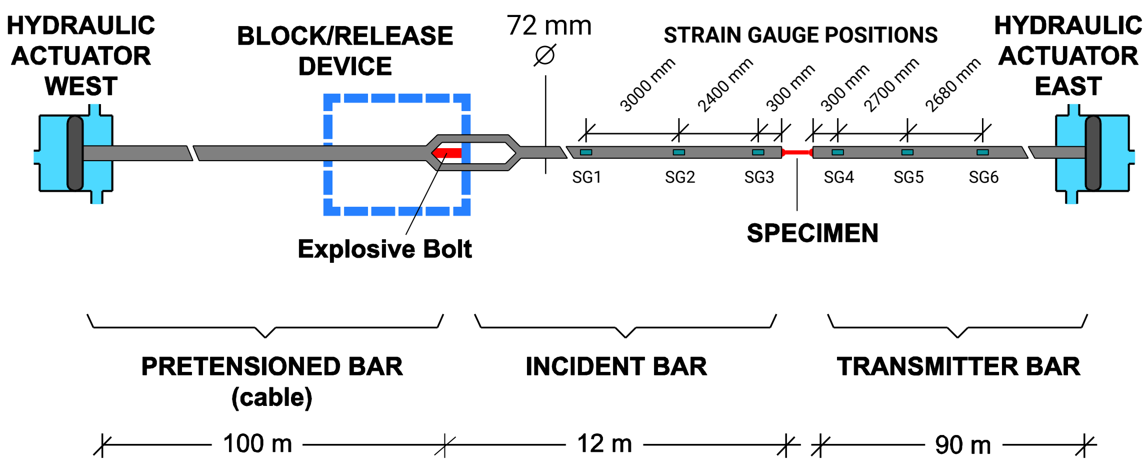

Figure 3: Schematic of the large Split Hopkinson bar for dynamic mechanical testing at the HopLab facility

Incident and transmission bars were equipped with six semiconductor strain-gauges connected in a full-bridge configuration. The positions of the strain gauges are illustrated in Figure 3. The Wheatstone bridge signal was amplified using a strain-gauge amplifier with a cut-off frequency of 500 kHz (EFS SGA02 high-speed) and then recorded at a sample-rate of 5 MHz with a fast transient recorder (National Instruments PXIe-1071 and acquisition boards PXIe-6366). The gain of the ohmic strain-gauges was increased to improve the sensitivity of the strain measurement in the output bar. In addition to measuring strain using gauges, a 2D digital image correlation system was used to capture the strain field in the specimens under loading [27]. A high-speed camera (Photron SA1.1) was used to capture the deformation of the specimens at 50,000 frames per second and at a resolution of 512 x 208 pixels. Cold lights (Veritas Constellation 120) were used to illuminate the specimen surface during the test. Figure 4 illustrates the imaging setup for the SHB tests. The specimens were speckled by hand using a white marker, resulting in an average speckle diameter of 1 mm. Given the resolution of the camera, this resulted in approximately 5 pixels per speckle, above the 3 pixel per speckle threshold required to avoid anti-aliasing issues [28]. Post-processing of the DIC images was conducted using the MatchID software package. Subset and step size were set to 15 and 17, respectively, and interpolation was conducted using a bi-cubic spline algorithm. Strains were determined using a filter size of 15. The noise floor was estimated to be 50 microstrain, based on the standard deviation of the axial strain in an image of an unstressed specimen. The spatial resolution of the DIC system — estimated on the basis of the subset, step, and strain filter size — was 3 mm.

Figure 4: DIC setup for the SHB experiments. The image on the left illustrates the camera positioning orthogonal to the specimen surface. The image on the right illustrates the lighting setup for the experiments and the DIC speckle.

Signals from the strain gauges were post-processed in MATLAB. Figure 5(a) illustrates the raw signals from the 6 semiconductor strain gauges adhered to the input and output bars. Note there is a slight offset of the force at time 0 due to the static preload of the bar. The resulting incident, transmitted and reflected waves, illustrated in Figure 5(b), were calculated using a deconvolution algorithm capable of compensating for wave dispersion distortions [29]. Oscillations in the input force history can be attributed to small propagation errors from the deconvolution algorithm and to the interaction of the stress waves with the specimen clamps. The applied strain-rate is plotted in Figure 6(a). The force-time data were combined with the displacement-time data obtained using DIC to generate force-displacement curves. Linear interpolation was used to account for the higher data recording frequency of the strain sensors relative to the high speed cameras. Note that due to the high sensitivity and low signal noise of the semiconductor strain gauges, it was not necessary to filter or smooth the raw signal data to obtain clear force-displacement and stress-strain plots.

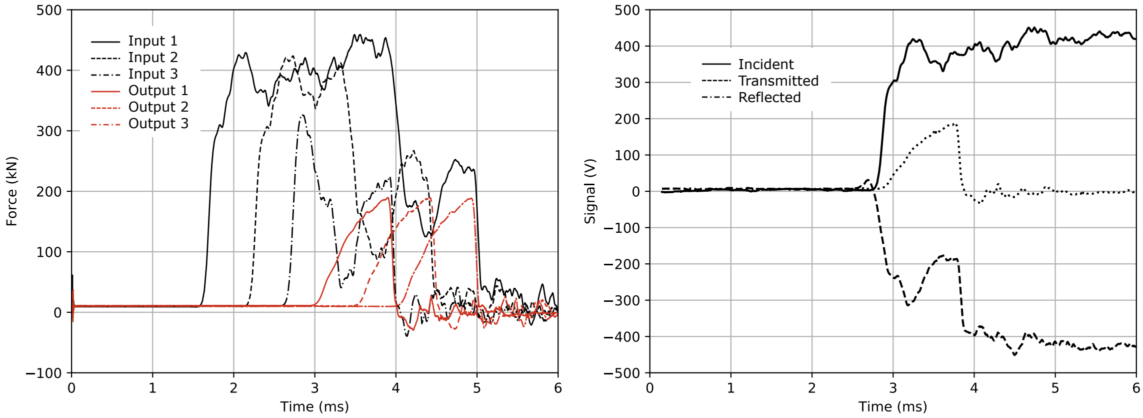

Figure 5: Raw semiconductor strain gauge signals (a) and the resulting waves (b) calculated using a deconvolution algorithm. for QI AP-PLY specimen 2.

The dynamic force equilibrium between bars was analyzed to validate the stress-strain curves. Figure 6(a) plots the force in the input and output bars against time for one of the cross-ply specimens. Despite the noise of the input bar signal, force equilibrium is reached in the 0.50 ms to 1.25 ms time interval. Analysis of the strains in the specimen at the input and output ends using DIC confirms the state of equilibrium in the specimen during the test, see Figure 6(b).

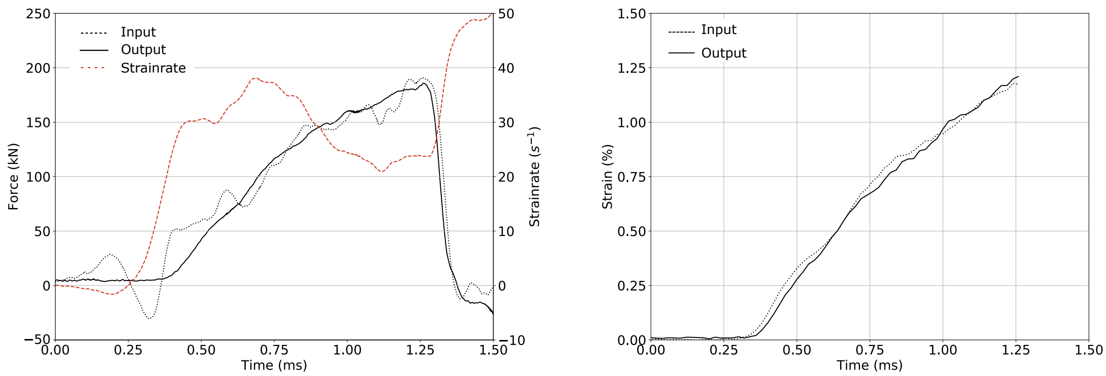

Figure 6: Validation of state of equilibrium for QI AP-PLY specimen 2: (a) input and output bar forces and strain rate as measured using SHB strain gauges, and (b) strain at the input and output ends, determined using DIC.

4. Numerical Simulations

The SHB experiments of the AP-PLY laminates were simulated using a previously developed multiscale continuum damage mechanics (CDM) framework [5], able of capturing the effects of the through thickness tow undulations on the macroscale laminate behavior. The model was previously validated for quasi-static tensile loading and is briefly recalled here for the sake of completeness.

4.1. Multiscale Constitutive Model

The approach divides AP-PLY laminates into regions of three different types; straight tow, resin-rich, and undulation. The region types are illustrated in Figure 7. Straight tow regions behave like conventional unidirectional composite laminae, resin-rich regions represent the edges of AFP tows where the fiber volume fraction is relatively low, and undulation regions represent the areas in an AP-PLY laminate where there is through thickness reinforcement. Unit cells are defined for each region, consisting of different volume fractions of micro constituents (tow or resin). Using an isostrain assumption, the strains on an element can be applied to each of its micro constituents. After the strains are rotated to the material coordinate system, a CDM model is used to determine the resulting stress in each micro-constituent. The stress-strain response of each element is determined by homogenizing the response of each of its micro-constituents. Using this approach it is possible to account for the effects of resin pockets and through thickness fiber undulation without modeling them explicitly geometrically, considerably reducing computational costs compared with purely micromechanical models [5].

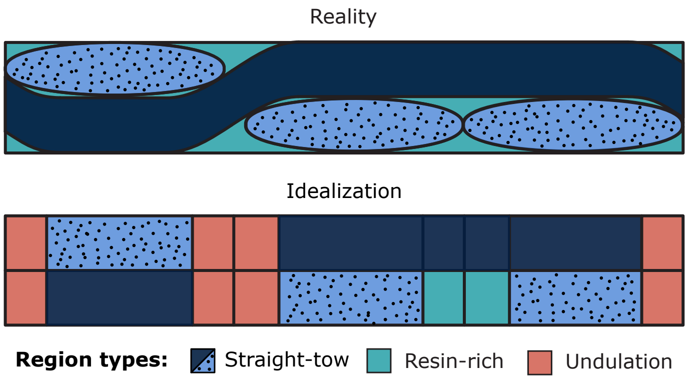

Figure 7: Illustration of the division of the AP-PLY geometry into idealized regions

Two constitutive models are defined; one for the pure resin constituent, and one for the resin impregnated fiber tows. The CDM model for the fiber tows is adapted from the work of Shah *et al.*, Maimi *et al.*, and Tan *et al.* [30, 31, 32, 33]. Prior to damage initiation, material behavior is defined as linear elastic. In the fiber direction, the onset of damage is predicted using maximum strain criteria, while matrix damage initiation is governed by a 3D adaptation of the Hashin failure criteria (Equations 1 - 6).

$$F^{1\mathrm{T}} = \frac{\varepsilon_{11}}{\varepsilon_{11}^{0\mathrm{T}}} \tag{1}$$

$$F^{1\mathrm{C}} = \frac{\varepsilon_{11}}{\varepsilon_{11}^{0\mathrm{C}}} \tag{2}$$

$$F^{2\mathrm{T}} = \left(\frac{\langle\widehat{\sigma}_{22}\rangle}{Y_{\mathrm{is}}^{\mathrm{T}}}\right)^2 + \left(\frac{\widehat{\tau}_{12}}{S_{\mathrm{is}}^{L}}\right)^2 + \left(\frac{\widehat{\tau}_{23}}{S^{\mathrm{T}}}\right)^2 \tag{3}$$

$$F^{2\mathrm{C}} = \left(\frac{\langle-\widehat{\sigma}_{22}\rangle}{2S^{\mathrm{T}}}\right)^2 + \left[\left(\frac{Y^{\mathrm{C}}}{2S^{\mathrm{T}}}\right)^2 - 1\right]\frac{\widehat{\sigma}_{22}}{Y^{\mathrm{C}}} + \left(\frac{\widehat{\tau}_{12}}{S_{\mathrm{is}}^{L}}\right)^2 \tag{4}$$

$$F^{3\mathrm{T}} = \left(\frac{\langle\widehat{\sigma}_{33}\rangle}{Z_{\mathrm{is}}^{\mathrm{T}}}\right)^2 + \left(\frac{\widehat{\tau}_{31}}{S_{\mathrm{is}}^{\mathrm{R}}}\right)^2 + \left(\frac{\widehat{\tau}_{23}}{S^{\mathrm{T}}}\right)^2 \tag{5}$$

$$F^{3\mathrm{C}} = \left(\frac{\langle-\widehat{\sigma}_{33}\rangle}{2S^{\mathrm{T}}}\right)^2 + \left[\left(\frac{Z^{\mathrm{C}}}{2S^{\mathrm{T}}}\right)^2 - 1\right]\frac{\widehat{\sigma}_{33}}{Z^{\mathrm{C}}} + \left(\frac{\widehat{\tau}_{31}}{S_{\mathrm{is}}^{\mathrm{R}}}\right)^2 \tag{6}$$

where $Y_{\mathrm{is}}^{\mathrm{T}}$, Y^{C}, $Z_{\mathrm{is}}^{\mathrm{T}}$, and Z^{C} are the tensile and compressive strengths in the transverse and through-thickness directions, respectively, and S_{is}^{L}, S^{T}, $S_{\mathrm{is}}^{\mathrm{R}}$ are the shear strengths in the 12, 23, and 31 directions, respectively. The is subscript indicates in-situ strengths [34, 35] and $\hat{\cdot}$ indicates a trial stress component.

After the onset of damage, material stiffness is degraded according to energy based damage evolution laws. In the fiber direction, damage evolution is exponential. The scalar damage variables can be expressed in the general form as (adapted from [36]):

$$d_1^{\mathrm{k}} = 1 - \frac{1}{f_1^{\mathrm{k}}\left(r_1^{\mathrm{k}}\right)} \exp\left\{A_1^{\mathrm{k}}\left[1 - f_1^{\mathrm{k}}\left(r_1^{\mathrm{k}}\right)\right]\right\} f\left(r_H\right) \quad \mathrm{k} = \mathrm{T}, \mathrm{C} \tag{7}$$

where r_1^{k} represents the elastic domain threshold, and A_1^{k} is a parameter ensuring the energy dissipated by the element is equal to the fracture energy of the material in the corresponding mode. The function $f_1^{\mathrm{k}}\left(r_1^{\mathrm{k}}\right)$ is used to force the softening of the constitutive relation, and function $f\left(r_N\right)$ couples the damage laws to the elastic domain thresholds.

In the transverse and through thickness directions damage accumulation results in linear softening of the modulus in the corresponding mode. The damage variables are expressed as functions of the ultimate failure strain ε^{f}, the strain at damage onset ε^0, and the current strain ε:

$$d = \frac{\varepsilon^{\mathrm{f}}\left(\varepsilon - \varepsilon^0\right)}{\varepsilon\left(\varepsilon^{\mathrm{f}} - \varepsilon^0\right)} \tag{8}$$

where the ultimate failure strain is dependent on; the fracture energy of the material $\mathcal{G}_c$ in the relevant direction, the characteristic length ℓ_c, and the stress at damage initiation σ^0.

The pure resin damage model assumes material behavior is isotropic. As such stiffness is degraded using a single scalar damage variable d_m. Damage onset is predicted using pressure dependent loading functions adapted from the work of Liu *et al.* [37].

$$F_m^{\mathrm{T}} = \frac{3J_2 + I_1\left(Y^{\mathrm{C}} - Y^{\mathrm{T}}\right)}{Y^{\mathrm{C}}Y^{\mathrm{T}}} \text{ if } I_1 \geq 0 \tag{9}$$

$$F_m^{\mathrm{C}} = -\frac{3J_2 + I_1\left(Y^{\mathrm{C}} - Y^{\mathrm{T}}\right)}{Y^{\mathrm{C}}Y^{\mathrm{T}}} \text{ if } I_1 < 0 \tag{10}$$

where I_1 represents the trace of the stress tensor and and J_2 is the second invariant of the deviatoric stress tensor. Y^{T} and Y^{C} are assumed to be equal to the tensile and compressive transverse strengths of the unidirectional tows. After failure initiation, moduli are degraded according to an exponential damage evolution laws similar to those used to express softening in the longitudinal damage modes of the impregnated fiber tow regions, see Equation 7.

4.2. FEA Implementation

The multiscale simulation framework presented above was implemented as a VUMAT subroutine in the finite element software Abaqus/Explicit. The geometry creation pre-processing scripts and the multiscale CDM subroutine are available on GitHub [1]. The quasi-static material properties of the prepreg fiber tows, shown in Table 1, were obtained experimentally according to the relevant standards, with the exception of the fracture toughnesses, which were taken from the literature [38, 39].

[1]`https://github.com/rutger-kok`

Table 1: Quasi-static Mechanical properties of SHD Composites VTC401 Prepreg [5].

Elastic Properties	E_{11} = 124.35 GPa, E_{22} = E_{22} = 7.23 GPa, G_{12} = G_{31} = 3.268 GPa, G_{23}= 2.638 GPa, $\nu_{12} = \nu_{31} = 0.339$, $\nu_{23} = 0.374$
Strengths	X^{T} = 2550 MPa, X^{C} = -1102 MPa, $Y^{\mathrm{T}} = Z^{\mathrm{T}}$ = 44 MPa, $Y^{\mathrm{C}} = Z^{\mathrm{C}}$ = -184 MPa, $S^{12} = S^{31}$ 55 MPa, S^{23} = 83 MPa
Fracture Energies	$\mathcal{G}_1^{\mathrm{T}}$ = 134 N/mm, $\mathcal{G}_1^{\mathrm{C}}$ = 95.0 N/mm, $\mathcal{G}_2^{\mathrm{C}}$ = 0.38 N/mm, $\mathcal{G}^6$ =1.62 N/mm

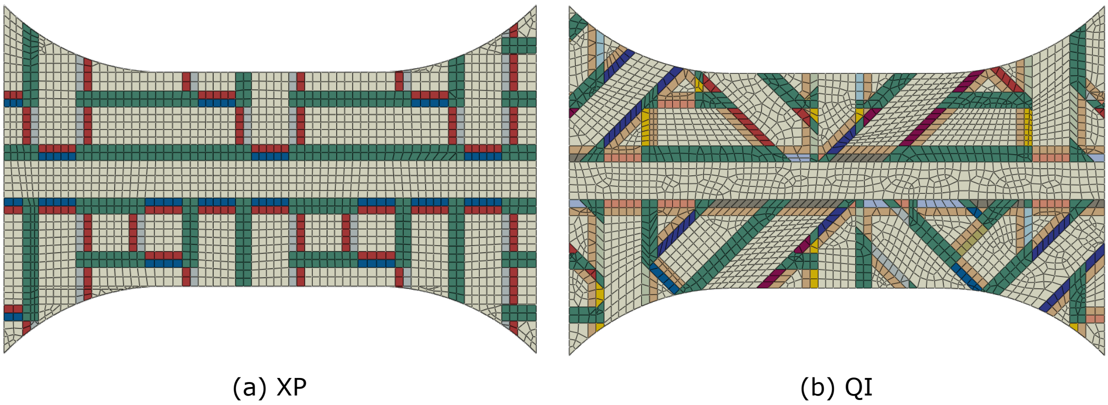

Figure 8: Finite element method meshes for the (a) cross-ply and (b) quasi-isotropic AP-PLY dogbone specimens.

Specimens were discretized using 8 node reduced integration linear solid C3D8R elements. Since the stacking sequence in each specimen is repeated and symmetric, an 8-ply sub-laminate was sufficient to represent the response of each 20-32 ply laminate. To further reduce computational cost, only the central (non-clamped) portion of the specimens was modeled. Elements sizes of approximately 1.5 mm were chosen to match the size of the mesoscale unit cells, whose dimensions are a function of the length of the tow undulations. This optimal element size ensured a realistic macro-to-meso strain transformation [30]. Note, however, that due to the automated partitioning of the specimens by the geometry generation scripts, some of the elements were smaller than the mesoscale unit cell. The specimen meshes are illustrated in Figure 8.

A zero displacement boundary condition was applied to the left hand side of each of the specimens. A relative velocity boundary condition was applied to the other end based on the input and output bar velocities measured experimentally by the strain gauges, see Figure 9. This approach, previously validated in studies of titanium alloys [40] and woven composites [41], is computationally efficient as it does not require the simulation of the entire SHB system. To avoid numerical instability issues at the onset of damage, Abaqus' default bulk viscosity option was used, and enhanced hourglass and distortion control were enabled. The energies in the simulation were monitored to ensure the artificial strain energy resulting from the section controls did not exceed 2% of the

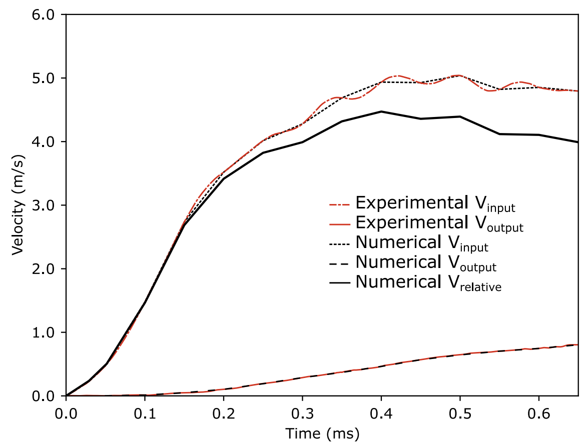

Figure 9: Experimental and numerical input and output bar velocities used to define the boundary conditions in the numerical simulations.

total energy in the system. The kinetic energy represented, on average, 0.6% of the total energy in the model. An element deletion criterion based on the determinant of the deformation gradient was implemented to prevent unrealistic element distortion resulting from the strain-softening constitutive behavior [42].

$$\text{Delete element if } \Big\{ \; 0 < \; \det \mathbf{F} < 0.5 \text{ or } \det \mathbf{F} > 2.5 \tag{11}$$

5. Results and Discussion

5.1. Dynamic response of AP-PLY composites

This section analyzes the performance of AP-PLY composites at high strain rates by considering the results of the experimental and numerical studies together. Figure 10 presents the experimental and numerical stress-strain response of the AP-PLY specimens subjected to tensile loading at an average strain rate of 30 s^{-1}. Despite the interaction of secondary waves and the initial noise of the pulse, the experiments show good repeatability, see Table 2. The moduli of the specimens were estimated over the strain interval from 0.4% to 0.8%, after dynamic force equilibrium was established and avoiding the non-linear response outside of this strain range.

Numerical models exhibit good agreement with the experimental results. Predictions of the strengths of the cross-ply and quasi-isotropic specimens are within the experimental error bounds, differing by -5.2% and 7.0% from the experimental values, respectively. The discrepancy between the numerical prediction and experimentally determined quasi-isotropic stiffness is similarly small at only -1.3%. In all specimens, baseline and AP-PLY, the gradient of the stress-strain response increases incrementally at strains of around 0.2 - 0.4%, a phenomenon not registered at material level by the numerical model. Rather than reflecting a change in material behavior, the change in slope, which occurs before dynamic equilibrium is established, is thought to result from localized stress concentrations in the clamped area. These concentrations resulted in the premature failure of 4 cross-ply specimens in the bolted joints of the grips instead of in the gauge section. Micro-inertial effects during dilation of the specimen, as discussed in [43], are hypothesized not to have affected the dynamic stress-strain response over the interval n which moduli were measured, as the specimens had all attained a state of dynamic force equilibrium at this point, and therefore accelerations within the specimens were likely to be negligible.

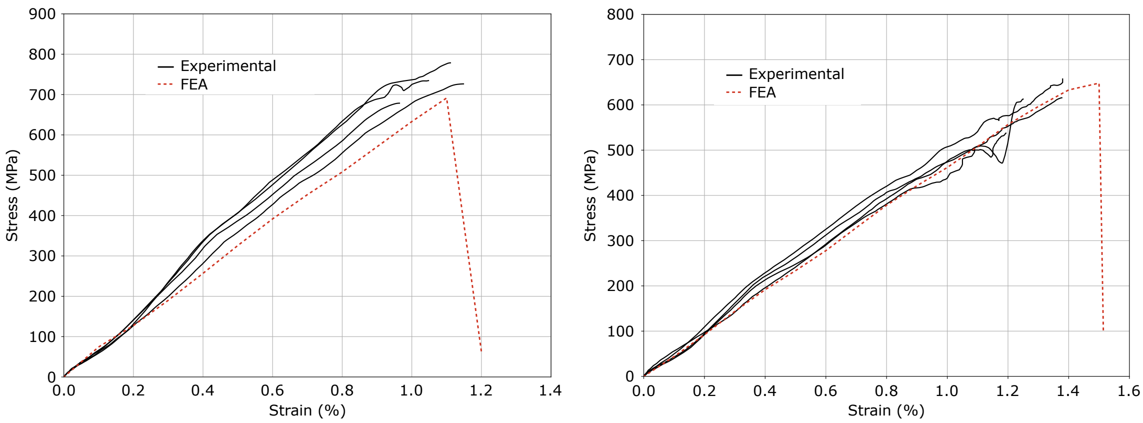

(a) Cross-ply

(b) Quasi-isotropic

Figure 10: Comparison of experimental and numerically predicted stress-strain dynamic response of AP-PLY (a) cross-ply and (b) quasi-isotropic laminates.

Table 2: Experimental and numerical results of AP-PLY composites at high strain rates.

Conf.	Modulus (GPa)		Strength (MPa)	
	Experimental	Numerical	Experimental	Numerical
$XP_{\text{AP-PLY}}$	69.38 ± 3.29	64.91	729.57 ± 35.48	691.51
$QI_{\text{AP-PLY}}$	47.41 ± 2.63	46.78	605.89 ± 43.19	648.11

Fig. 11 and 12 compare the experimental and numerical evolution of the strain fields for AP-PLY laminates. The symmetry of the strain field measured using DIC, in which similar strain values are measured at both clamped edges, lends further credence to the assumption of force equilibrium in the specimen. The strain fields measured on the surface of the specimens depend on each laminate's stacking sequence. The cross-ply laminate's strain field is homogeneous over the central region, but strain gradients develop at the shoulders of the specimen (Figure 11). In contrast, the quasi-isotropic strain field is more heterogeneous, with higher strains occurring in an hourglass shaped region in the center of the specimen (Figure 12).

The simulations are able to capture the overall macro-deformation of the specimens, as well as the location and size of the strain micro-gradients at the tow undulations. These microgradients have been previously registered experimentally during quasi-static testing [5]. In the present work, the resolution of the DIC system was insufficient to capture the strain gradients at the tow undulations. As mentioned in section 3 the spatial resolution of the DIC system was approximately 3 mm, in excess of the size of the undulation regions, of approximately 1.5 mm.

The damage mechanisms are effectively captured by the numerical models. Matrix cracking initiates in undulation regions near the specimen shoulders at approximately 0.6% nominal strain. Localized matrix softening places additional stress on the fiber tows in these areas, inducing fiber

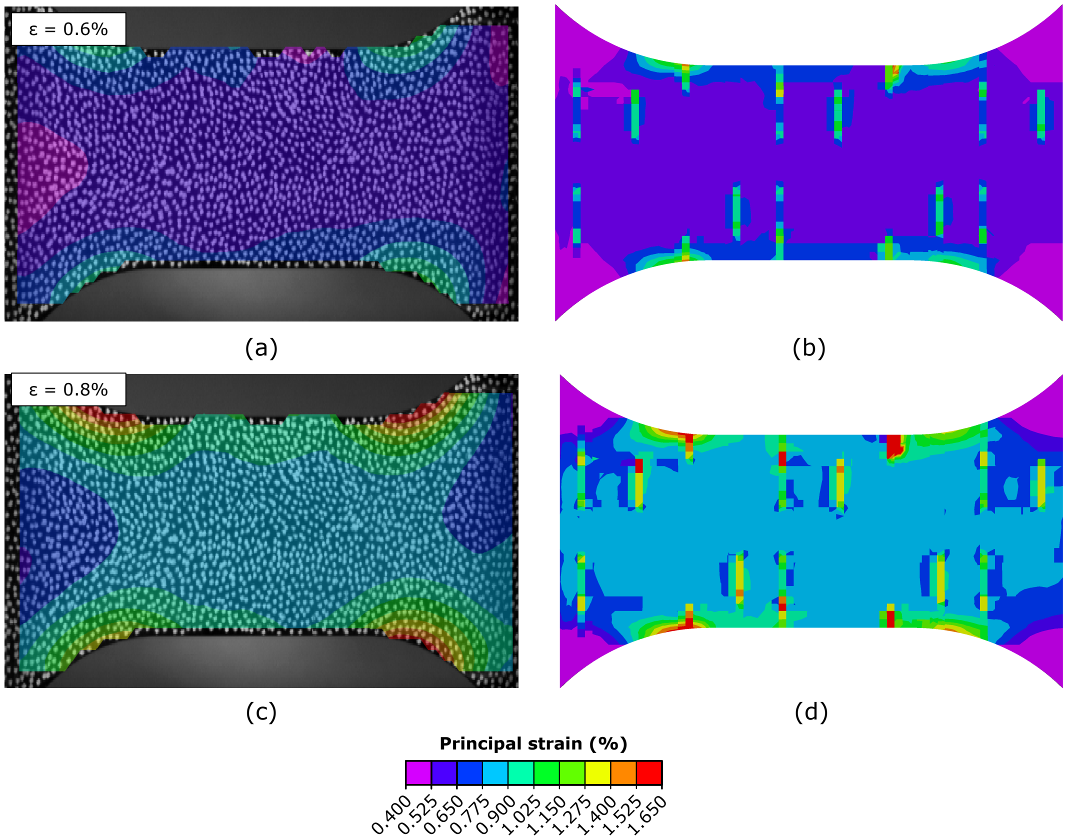

Figure 11: Experimental (a) & (c) and numerical (b) and (d) principal strain contours on cross-ply AP-PLY specimens at 0.6% and 0.8% nominal strain.

fracture. In the cross-ply specimens, catastrophic failure through fiber fracture occurs on a plane orthogonal to the loading direction, near the specimen shoulder, see Figure 13. In the quasi-isotropic specimens, the failure surface is v-shaped (i.e. at 45°angles to the loading direction), a phenomenon which is reflected in the experimental results, see Figure 14. Equally well represented is the extensive matrix damage occurring in the vicinity of the fracture plane.

5.2. Influence of undulations at high strain rates

Table 3 summarizes the experimental results at quasi-static and dynamic strain rates. It includes both stacking sequences (cross-ply and quasi-isotropic) and also compares AP-PLY and baseline laminates. The quasi-static results were obtained from a previous study by the same

Table 3: Quasi-static vs dynamic laminate moduli and strengths.

Configuration	**Modulus [GPa]**		**Strength [MPa]**	
	$25 \times 10^{-4} s^{-1}$	$30\ s^{-1}$	$25 \times 10^{-4} s^{-1}$	$30\ s^{-1}$
$\mathrm{XP}_{\text{AP-PLY}}$	65.27 ± 3.53	69.38 ± 3.29	1060.31 ± 47.55	729.57 ± 35.48
$\mathrm{XP}_{\text{base}}$	63.59 ± 1.23	62.01 ± 3.63	1273.16 ± 55.61	683.58 ± 68.03
$\mathrm{QI}_{\text{AP-PLY}}$	44.96 ± 0.57	47.41 ± 2.63	705.67 ± 28.85	605.89 ± 43.19
$\mathrm{QI}_{\text{base}}$	44.56 ± 0.95	43.88 ± 1.51	655.90 ± 29.79	601.23 ± 38.47

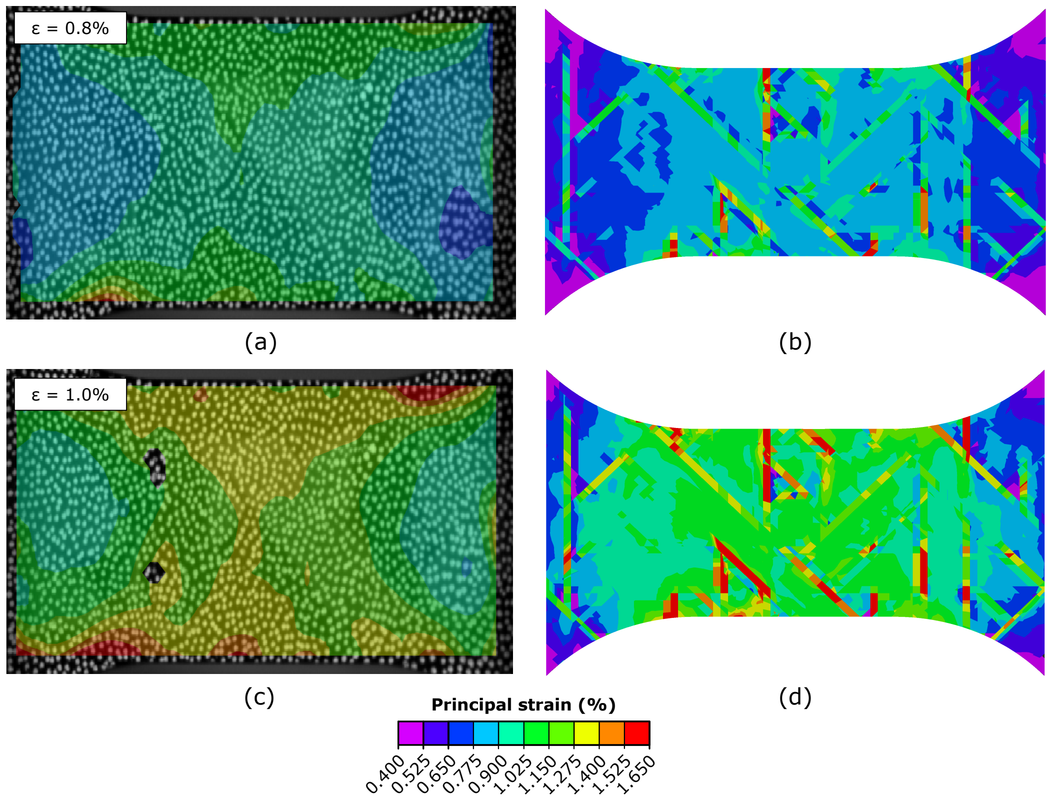

Figure 12: Experimental (a) & (c) and numerical (b) and (d) principal strain contours on quasi-isotropic AP-PLY specimens at 0.8% and 1.0% nominal strain.

authors [5]. It should be noted that the dimensions of the specimens studied in the quasi-static regime differed from those in the dynamic regime. In the former, the specimens were adapted from the ISO 527 standard, and measured 250 mm in length, 40 mm in width, and approximately 1.6 mm in thickness.

Given the overlapping error bounds, we conclude there is no significant difference between the moduli of the AP-PLY specimens at high and low strain rates. Similarly, there is no appreciable strain rate dependency in the baseline laminates. Figure 15 presents the quasi-static and dynamic response of the AP-PLY and baseline laminates. In the dynamic regime, there are marginal improvements in laminate stiffness resulting from the AP-PLY preforming process. However, given the complexity of the dynamic experiments and the intrinsic oscillations in the stress-strain response, the discrepancy may be the result of experimental scatter alone. The same conclusion was drawn at quasi-static strain rates, where the preforming process also had a negligible impact on the stiffness of the laminates [5]. As previously acknowledged, the dimensions of the specimens tested in the quasi-static and dynamic regime differed. It is well known that larger specimen sizes may result in lower strengths, especially for specimens tested in tension [44]. To evaluate whether this was the case in the present study, a small number of quasi-static tests were conducted using specimens identical to those used in the high strain rate tests. Failure strengths and moduli for these specimens were within 10% of the experimental results obtained using the smaller specimens.

The strength of all the specimens, both AP-PLY and baseline, is significantly reduced at high

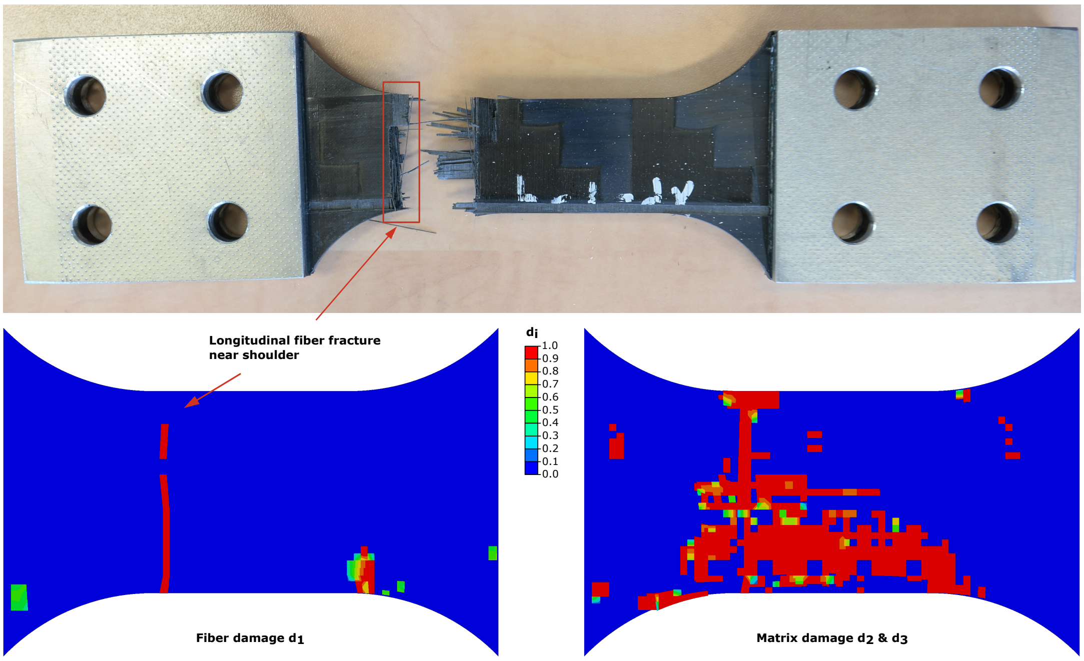

Figure 13: Experimentally observed failure modes and simulated damage envelopes in a cross-ply AP-PLY laminate.

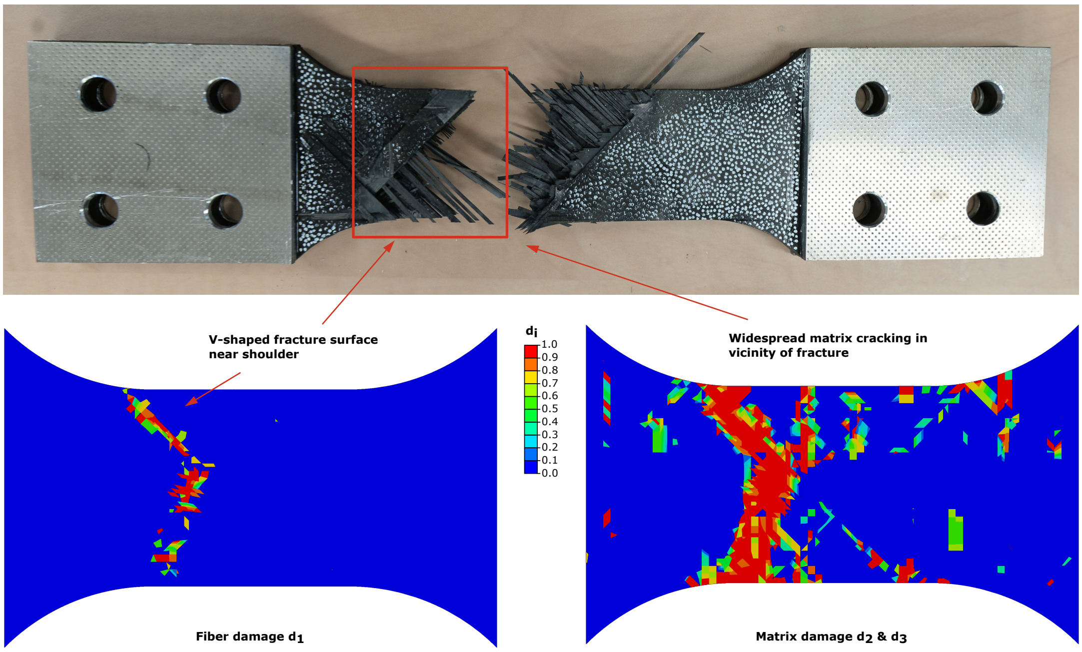

Figure 14: Experimentally observed failure modes and simulated damage envelopes in a quasi-isotropic AP-PLY laminate.

strain rates. The proximity of the failure plane to the specimen shoulders, and the strain concentrations measured using DIC, suggest that this lower strength may be a consequence of the geometry of the specimens, rather than strain rate dependency at the material level. As mentioned previously, brittle carbon fiber composites are sensitive to mechanical gripping at high strain rates, potentially reducing their measured strength [20]. Moreover, while stress concentrations arising from the through-thickness reinforcements in the cross-ply AP-PLY laminates *could* trigger failure

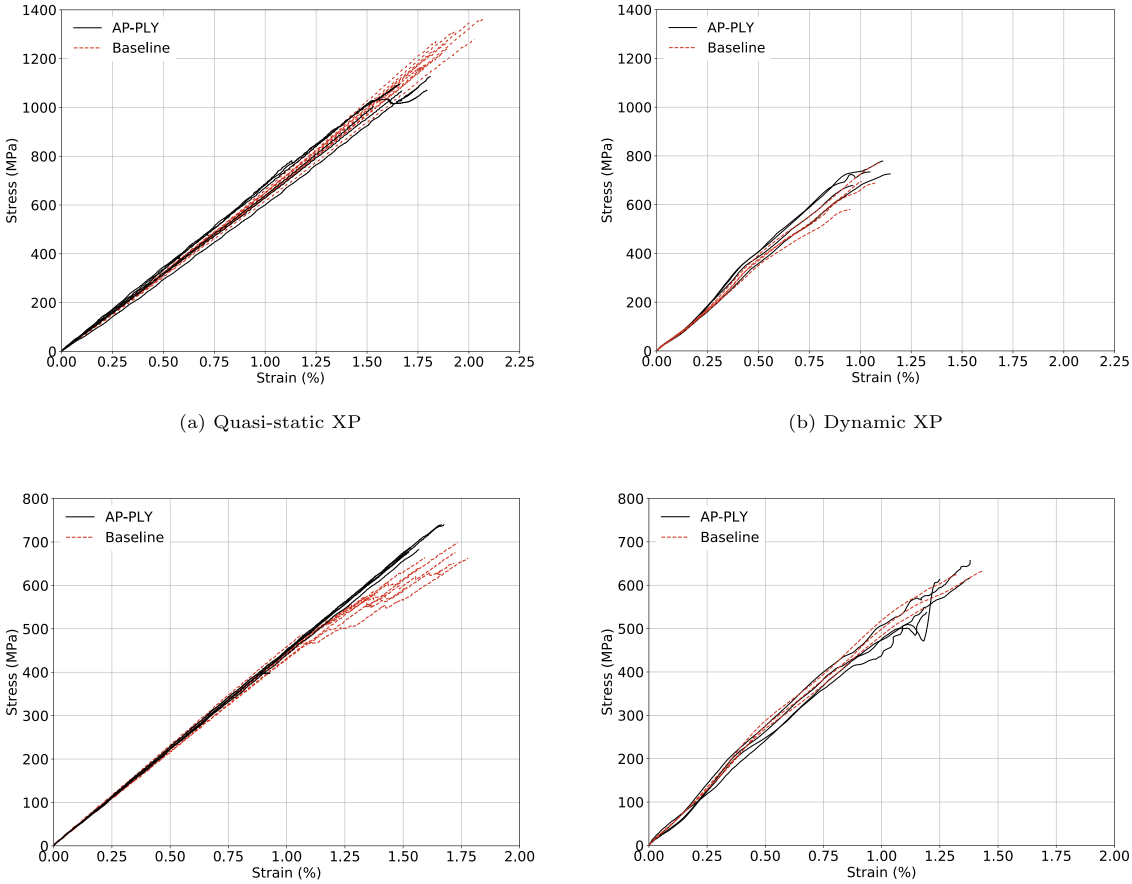

(a) Quasi-static XP

(b) Dynamic XP

(c) Quasi-static QI

(d) Dynamic QI

Figure 15: Stress-strain response of (baseline and AP-PLY) cross-ply and quasi-isotropic laminates under quasi-static (a) & (c) and dynamic (b) & (d) loading.

in the specimens at relatively low loads, the fact that the strength of the baseline laminates was reduced to a similar or greater extent suggests that the fiber undulations are not the primary cause of the low dynamic tensile strength. The reduction in the quasi-isotropic specimen strength at high strain rates is less substantial compared with the cross-ply specimens. The high strain rate strengths of the cross-ply baseline and AP-PLY specimens fell by 46% and 32% respectively, relative to their quasi-static strength, while the reduction in quasi-isotropic baseline and AP-PLY strengths were only 8% and 14% respectively. This is because, as illustrated in Figure 12, the strain concentrations at the shoulders of the quasi-isotropic specimen are less pronounced than in the cross-ply specimens. A possible explanation for the smaller magnitude of these strain concentrations is the greater distribution of tow orientations, and as a result the smaller mismatch angles between tows.

At high strain rates, the strengths of the cross ply AP-PLY laminates were found to be insensitive to the internal architecture. This contrasts with data from the quasi-static regime, in which the strength of cross-ply laminates was negatively affected (-17% loss) by the AP-PLY preforming process [5]. A plausible explanation for this result is that the through thickness undulations present in an AP-PLY laminate are more effective as crack arrestors in the dynamic than in the quasi-static regime. At low strain rates, undulating tows straighten along the loading direction as the specimens are stressed. This alignment progressively increases the magnitude of the strain gradients at the undulations, resulting in reductions to laminate strength. At high strains rates however, there is insufficient time for tow rotation to occur. As a result, the strain concentration factors at through thickness undulations are smaller, while the reinforcement that these features provide is unaffected. The through thickness connectivity in the laminate mitigates the formation and propagation of matrix cracks, delaying softening and improving the strength of the AP-PLY cross-ply laminates.

In contrast to the cross-ply results, the trends in quasi-isotropic laminate strength were similar for both high and low strain rate loading. In both the quasi-static and dynamic regimes, the discrepancy between the AP-PLY and baseline strengths was within the experimental error bounds, with the former generally exhibiting marginally higher strengths. The tow straightening effects hypothesized to occur in the cross-ply laminates are likely to be less significant in the quasi-isotropic composites, because the former contain a larger proportion of tows oriented with the loading direction, in which the aforementioned dynamic deformation mechanisms will be more significant, and because the mismatch angles between tows in the quasi-isotropic laminates are generally smaller, reducing the magnitude of the strain concentrations. Furthermore, in the AP-PLY laminates, matrix cracks formed predominantly at the boundaries between tows, rarely splitting a tow in the transverse direction. This contrasts with the more widespread matrix cracking observed in the baseline laminates, and may explain the slightly higher average strengths of the AP-PLY laminates in both loading regimes.

The numerical model predictions of stiffness and strength at both low and high strain rates are in good agreement with the experimental results, despite using strain rate independent material properties [5]. This suggests that the effect of the strain rate at the material level is minor, and that the realignment of the fibers may play a larger role. Carbon fiber epoxy composites are strain rate insensitive in the fiber direction [10, 45, 46], and at the relatively low dynamic strain rates attained in this study (30 s^{-1}), the transverse properties are likely to be only minimally affected [10, 46]. While microscale numerical modeling and/or in-situ high-speed synchrotron tomography might shed further light on the underlying causes of the discrepancy between the baseline and AP-PLY specimens at high strain rates, they are beyond the scope of this study. Note that at strain rates higher than those studied in the present work (30 s^{-1}), the strain rate sensitivity of the matrix or fibers may have a more significant effect on laminate behavior, and the inclusion of strain rate dependent material models may improve the accuracy of numerical simulation predictions.

In summary, these findings prove that the through thickness tow undulations present in an AP-PLY composite do not have a detrimental effect on its dynamic mechanical properties. Furthermore, through thickness undulation have the capacity to arrest cracks, delaying the propagation of delamination, and, depending on the laminate configuration, improving the laminate strength. This contrasts with AFP defects e.g. tow overlaps or tow gaps, which have been observed to reduce a composite's strength [47]. While overlaps and gaps are unpredictable features that occur randomly throughout a laminate, the through thickness undulations introduced by the AP-PLY process occur in a structured pattern and, more importantly, can be strategically distributed to improve the local damage tolerance of composite structures subjected to dynamic loads.

6. Conclusions

The high strain rate tensile behavior of AP-PLY composites was investigated. Due to the large representative volume elements and brittle nature of the laminates, experiments were conducted at the European Laboratory for Structural Assessment, one of the only laboratories worldwide capable of accurately analyzing this family of composite materials. The bespoke SHB equipment and the relatively low impedance design of the clamps ensured dynamic force equilibrium was rapidly established, providing accurate measurements even at low strains. In addition, the SHB experiments were simulated using a multiscale numerical modeling framework to gain further insight into the high strain rate deformation mechanisms of the novel pseudo woven composites.

Quasi-isotropic and cross-ply AP-PLY specimens were subjected to tensile loading at a strain rate of approximately 30 s^{-1}. The moduli of the AP-PLY composites were found to be independent of the strain rate. While the dynamic experimental AP-PLY laminate strengths were significantly less than the quasi-static strengths, this discrepancy was attributed to the geometry of the specimens and the resulting strain concentrations, rather than strain rate dependency in the constituent materials. Numerical model results provided further evidence that the material strength of the AP-PLY composites was not affected by the higher strain rate.

The response of the AP-PLY laminates was compared with baseline — non AP-PLY — laminates to quantify the effect of the three-dimensional reinforcement. The through thickness undulations introduced by the AP-PLY preforming process did not result in a reduction in laminate stiffness in the dynamic regime. While the dynamic AP-PLY laminate moduli were found to be greater than those of the baseline laminates, the discrepancies were small, and could be attributed to the resolution of the SHB equipment. In terms of strength, different trends were obtained depending on the predominant failure micromechanism. The failure of the quasi-isotropic AP-PLY laminates was dominated by localized matrix cracking at the tow boundaries regardless of the applied strain rate. This mechanism promoted tow debonding rather than the extensive matrix cracking observed in the baseline laminates, showing the capacity of the AP-PLY architecture to influence laminate deformation. As a result, the quasi-isotropic AP-PLY laminates exhibited slightly higher strengths than their baseline non AP-PLY counterparts at both high and low strain rates. In the cross-ply AP-PLY laminates, strain concentrations at through thickness undulations were found to be the catalysts for failure at low strain rates. In the dynamic regime however, these concentrations had a much smaller impact on the laminate response. This change in behavior was attributed to reduced out-of-plane tow straightening, resulting in smaller strain gradients at tow undulations. As a result, the reduction in cross-ply AP-PLY laminate strength, relative to the baseline, registered in the quasi-static loading regime, was not observed at high strain rates.

In summary, at high strain rates, the strain concentrations induced by the geometry of the individual tapes at through thickness undulations and tow boundaries were less significant. As a result, no reduction in AP-PLY stiffness nor strength in comparison to the baseline laminates was obtained. These results prove AP-PLY laminates are effective substitutes for conventional angle-ply laminates in dynamic loading scenarios. They possess the same exceptional specific stiffness as angle-ply laminates, while their improved damage tolerance at high strain rates can result in higher strengths — depending on the stacking sequences. Future studies will investigate the low-velocity impact response of AP-PLY laminates.

7. Acknowledgements

The experimental data used in this research were generated through access to the ELSA HopLab under the Framework of access to the Joint Research Centre Physical Research Infrastructures of the European Commission (CATCH project, Research Infrastructure Access Agreement Nr. 35922-1/2018-1-RD-ELSA-HopLab). This research was also supported by the Royal Society (grant number RGS/R2/180091). The authors would like to acknowledge Dr. David Townsend and Dr. Karthik Ram Ramakrishnan for their contribution. The technical support of Mr. Edward Monteith is gratefully acknowledged. Finally, the authors would like to acknowledge Rolls-Royce plc for their continuous support through the Solid Mechanics University Technology Centre at the University of Oxford.

References

[1] M. H. Nagelsmit, *Fibre Placement Architectures for Improved Damage Tolerance*. PhD thesis, Delft University of Technology, 2013.

[2] C. V. Rad, F. Thomas, S. Sockalingam, and Z. Gurdal, "Low Velocity Impact Response of Hybrid Pseudo-Woven Fiber-Reinforced Composite Laminates," in *International SAMPE Technical Conference*, (Charlotte, North Carolina), SAMPE, 2019.

[3] X. Li, J. Dufty, and G. M. Pearce, "Automation of tow wise modelling for automated fibre placement and filament wound composites," *Composites Part A: Applied Science and Manufacturing*, vol. 147, no. April, p. 106449, 2021.

[4] X. Li, S. A. Brown, M. Joosten, and G. M. Pearce, "Tow Wise Modelling of Non-conventional Automated Fibre Placement Composites: Short Beam Shear Study," *Composites Part A: Applied Science and Manufacturing*, vol. 154, no. December 2021, p. 106767, 2021.

[5] R. Kok, F. Martinez-Hergueta, and F. Teixeira-Dias, "Tensile response of AP-PLY composites: A multiscale experimental and numerical study," *Composites Part A: Applied Science and Manufacturing*, vol. 159, no. 106989, 2022.

[6] C. V. Rad, F. D. Thomas, B. Seay, and M. J. L. V. Tooren, "Manufacturing and characterization of novel clutch non-conventional fiber- reinforced composite laminates," *Composite Structures*, vol. 215, no. September 2018, pp. 454–470, 2019.

[7] B. Waddington, A. Silva-Caballero, S. Roy, W. Kennon, and P. Potluri, "Damage tolerance of Carbon/Epoxy quasi-interwoven composites subjected to low velocity impacts," *21st International Conference on Composite Materials*, no. August, pp. 20–25, 2017.

[8] C. V. Rad, K. Kodagali, J. Roark, D. Revilock, C. Ruggeri, R. Harik, and S. Sockalingam, "High velocity impact response of hybridized pseudo-woven carbon fiber composite architectures," *Composites Part B: Engineering*, vol. 203, no. October, p. 108478, 2020.

[9] A. Graziano, O. A. Titton Dias, and O. Petel, "High-strain-rate mechanical performance of particle- and fiber-reinforced polymer composites measured with split Hopkinson bar: A review," *Polymer Composites*, vol. 42, no. 10, pp. 4932–4948, 2021.

[10] H. Koerber, J. Xavier, and P. P. Camanho, "High strain rate characterisation of unidirectional carbon-epoxy IM7-8552 in transverse compression and in-plane shear using digital image correlation," *Mechanics of Materials*, vol. 42, no. 11, pp. 1004–1019, 2010.

[11] H. Koerber, J. Xavier, P. P. Camanho, Y. E. Essa, and F. Martín De La Escalera, "High strain rate behaviour of 5-harness-satin weave fabric carbon-epoxy composite under compression and combined compression-shear loading," *International Journal of Solids and Structures*, vol. 54, pp. 172–182, 2015.

[12] H. Cui, D. Thomson, A. Pellegrino, J. Wiegand, and N. Petrinic, "Effect of strain rate and fibre rotation on the in-plane shear response of 45 laminates in tension and compression tests," *Composites Science and Technology*, vol. 135, pp. 106–115, 2016.

[13] H. Liu, H. Nie, C. Zhang, and Y. Li, "Loading rate dependency of Mode I interlaminar fracture toughness for unidirectional composite laminates," *Composites Science and Technology*, vol. 167, no. April, pp. 215–223, 2018.

[14] R. Gerlach, C. R. Siviour, J. Wiegand, and N. Petrinic, "In-plane and through-thickness properties, failure modes, damage and delamination in 3D woven carbon fibre composites subjected to impact loading," *Composites Science and Technology*, vol. 72, no. 3, pp. 397–411, 2012.

[15] Y. Wan, B. Sun, and B. Gu, "Multi-scale structure modeling of damage behaviors of 3D orthogonal woven composite materials subject to quasi-static and high strain rate compressions," *Mechanics of Materials*, vol. 94, pp. 1–25, 2016.

[16] M. Tarfaoui, M. Nachtane, and A. El Moumen, "Energy dissipation of stitched and unstitched woven composite materials during dynamic compression test," *Composites Part B: Engineering*, vol. 167, pp. 487–496, 2019.

[17] X. Chen, Y. Li, Z. Zhi, Y. Guo, and N. Ouyang, "The compressive and tensile behavior of a 0/90 C fiber woven composite at high strain rates," *Carbon*, vol. 61, pp. 97–104, 2013.

[18] A. Elmahdy and P. Verleysen, "Challenges related to testing of composite materials at high strain rates using the split Hopkinson bar technique," *EPJ Web of Conferences*, vol. 183, 2018.

[19] R. Gerlach, C. Kettenbeil, and N. Petrinic, "A new split Hopkinson tensile bar design," *International Journal of Impact Engineering*, vol. 50, pp. 63–67, 2012.

[20] J. Zhou and V. L. Tagarielli, "On the Development of New Test Techniques to Measure the Tensile Response of Materials at High and Ultra-high Strain Rates," *Experimental Mechanics*, vol. 62, no. 1, pp. 151–164, 2022.

[21] F. Martínez-Hergueta, A. Pellegrino, A. Ridruejo, N. Petrinic, C. González, and J. LLorca, "Dynamic tensile testing of needle-punched nonwoven fabrics," *Applied Sciences (Switzerland)*, vol. 10, no. 15, 2020.

[22] H. Zhao, "Material behaviour characterisation using SHPB techniques, tests and simulations," *Computers and Structures*, vol. 81, no. 12, pp. 1301–1310, 2003.

[23] M. Sasso, G. Newaz, and D. Amodio, "Material characterization at high strain rate by Hopkinson bar tests and finite element optimization," *Materials Science and Engineering A*, vol. 487, no. 1-2, pp. 289–300, 2008.

[24] P. Zivkovic, C. Ward, and G. Marengo, "Innovative preform design exploiting automated fibre placement," *ECCM 2018 - 18th European Conference on Composite Materials*, no. June, pp. 24–28, 2020.

[25] M. D. Hoang, J.-f. Simpson, and S. V. Hoa, "Laminates With Under / Over Lacing Made By Automated Fiber Placement," *21st International Conference on Composite Materials*, no. August, pp. 1–9, 2017.

[26] European Commission, "European Laboratory for Structural Assessment: Large Hopkinson Bar Facility (ELSA-HopLab)," 2020.

[27] G. Quino, Y. Chen, K. R. Ramakrishnan, F. Martínez-Hergueta, G. Zumpano, A. Pellegrino, and N. Petrinic, "Speckle patterns for DIC in challenging scenarios: Rapid application and impact endurance," *Measurement Science and Technology*, vol. 32, no. 1, 2021.

[28] P. Reu, "All about speckles: Aliasing," *Experimental Techniques*, vol. 38, no. 5, pp. 1–3, 2014.

[29] M. N. Bussac, P. Collet, G. Gary, and R. Othman, "An optimisation method for separating and rebuilding one-dimensional dispersive waves from multi-point measurements. Application to elastic or viscoelastic bars," *Journal of the Mechanics and Physics of Solids*, vol. 50, no. 2, pp. 321–349, 2002.

[30] S. Shah, P. Megat-Yusoff, S. Karuppanan, R. Choudhry, and Z. Sajid, "Multiscale damage modelling of 3D woven composites under static and impact loads," *Composites Part A: Applied Science and Manufacturing*, vol. 151, no. September, p. 106659, 2021.

[31] P. Maimí, P. P. Camanho, J. A. Mayugo, and C. G. Dávila, "A continuum damage model for composite laminates: Part I – Constitutive model," *Mechanics of Materials*, vol. 39, no. 10, pp. 897–908, 2007.

[32] P. Maimí, P. P. Camanho, J. A. Mayugo, and C. G. Dávila, "A continuum damage model for composite laminates: Part II – Computational implementation and validation," *Mechanics of Materials*, vol. 39, no. 10, pp. 909–919, 2007.

[33] W. Tan, B. G. Falzon, L. N. Chiu, and M. Price, "Predicting low velocity impact damage and Compression-After-Impact (CAI) behaviour of composite laminates," *Composites Part A: Applied Science and Manufacturing*, vol. 71, pp. 212–226, 2015.

[34] P. P. Camanho, C. G. Dávila, S. T. Pinho, L. Iannucci, and P. Robinson, "Prediction of in situ strengths and matrix cracking in composites under transverse tension and in-plane shear," *Composites Part A: Applied Science and Manufacturing*, vol. 37, no. 2, pp. 165–176, 2006.

[35] G. Catalanotti, P. P. Camanho, and A. T. Marques, "Three-dimensional failure criteria for fiber-reinforced laminates," *Composite Structures*, vol. 95, pp. 63–79, 2013.

[36] C. S. Lopes, S. Sádaba, C. González, J. Llorca, and P. P. Camanho, "Physically-sound simulation of low-velocity impact on fiber reinforced laminates," *International Journal of Impact Engineering*, vol. 92, pp. 3–17, 2016.

[37] G. Liu, L. Zhang, L. Guo, F. Liao, T. Zheng, and S. Zhong, "Multi-scale progressive failure simulation of 3D woven composites under uniaxial tension," *Composite Structures*, vol. 208, no. June 2018, pp. 233–243, 2019.

[38] E. J. Pappa, J. A. Quinn, E. D. Mccarthy, J. J. Murray, J. R. Davidson, and C. M. Ó Brádaigh, "Experimental Study on the Interlaminar Fracture Properties of Carbon Fibre Reinforced Polymer Composites with a Single Embedded Toughened Film," *Polymers*, vol. 13, no. 4103, 2021.

[39] C. Furtado, G. Catalanotti, A. Arteiro, P. J. Gray, B. L. Wardle, and P. P. Camanho, "Simulation of failure in laminated polymer composites: Building-block validation," *Composite Structures*, vol. 226, no. April, p. 111168, 2019.

[40] B. Cousins, *Development of improved numerical techniques for high strain rate deformation behaviour of titanium alloys*. PhD thesis, University of Oxford, 2016.

[41] F. Martínez-Hergueta, D. Ares, A. Ridruejo, J. Wiegand, and N. Petrinic, "Modelling the in-plane strain rate dependent behaviour of woven composites with special emphasis on the

non-linear shear response," *Composite Structures*, vol. 210, no. December 2018, pp. 840–857, 2019.

[42] B. G. Falzon and W. Tan, "Virtual Testing of Composite Structures: Progress and Challenges in Predicting Damage, Residual Strength and Crashworthiness," in *The Structural Integrity of Carbon Fiber Composites* (P. W. R. Beaumont, C. Soutis, and A. Hodzic, eds.), ch. 24, pp. 699–743, Cham: Springer International Publishing, 1 ed., 2017.

[43] E. A. De Souza Neto, P. J. Blanco, P. J. Sánchez, and R. A. Feijóo, "An RVE-based multiscale theory of solids with micro-scale inertia and body force effects," *Mechanics of Materials*, vol. 80, no. Part A, pp. 136–144, 2015.

[44] M. R. Wisnom, "Size effects in the testing of fibre-composite materials," vol. 59, pp. 1937–1957, 1999.

[45] J. Harding and L. M. Welsh, "A tensile testing technique for fibre-reinforced composites at impact rates of strain," *Journal of Materials Science*, vol. 18, no. 6, pp. 1810–1826, 1983.

[46] N. Taniguchi, T. Nishiwaki, and H. Kawada, "Tensile strength of unidirectional CFRP laminate under high strain rate," *Advanced Composite Materials: The Official Journal of the Japan Society of Composite Materials*, vol. 16, no. 2, pp. 167–180, 2007.

[47] A. Trochez, V. C. Jamora, R. Larson, K. C. Wu, D. Ghosh, and O. G. Kravchenko, "Effects of automated fiber placement defects on high strain rate compressive response in advanced thermosetting composites," *Journal of Composite Materials*, 2021.